Soft Robots Proprioception Through Stretchable Laser-Induced Graphene Strain Sensors

Giovanna De Luca, Anna Chiara Bressi, Radan Pathan, Niccolò Pagliarani, Martina Maselli, Francesco Greco, and Matteo Cianchetti**

Soft robotic grippers enable the safe manipulation of delicate objects, guaranteeing their integrity when handled and collected. Integrating sensors into these grippers can enable their proprioception but must avoid compromising flexibility or functionality. This study presents a pneumatic finger-based soft gripper with a novel piezoresistive sensor made of laser-induced graphene (LIG) embedded in dragon skin (DS), an elastomer matrix, offering continuous bending angle measurement. The LIG/DS composite is studied to confirm minimal impact on the gripper's stiffness. Mechanical and electromechanical characterizations are performed for two sensor designs, n_1 and n_2. Design n_1 exhibits superior performance, with a gauge factor $\mathrm{GF}_{n_1} = 87.5 \pm 1.83$, a linear response of up to 30% strain, and durability exceeding 10 000 cycles. A finite-element method analysis identifies the fingers' neutral bending plane, guiding optimal sensor placement. Experimental validation confirms theoretical predictions and finds the ideal sensor location, achieving a linear response up to 110° with low hysteresis (8%). The sensor enables real-time monitoring of finger bending during grasping tasks, with a calibration curve linking resistance changes to bending angles. This cost-effective, stretchable, and durable sensor demonstrates high potential for soft robotic applications, offering precise and reliable proprioception without compromising the gripper's soft properties.

1. Introduction

Grasping and manipulation of objects are fundamental abilities performed by humans, animals, and robots. Conventional robotic grippers, built primarily with rigid joints and links, often lack the flexibility needed for complex manipulation tasks.[1] In contrast, soft grippers composed of multiple fingers provide greater dexterity and reduce the risk of damaging delicate objects.[2] Accurate task execution in such soft robots relies on awareness of both internal (proprioceptive) and external (exteroceptive) states. Sensors are thus critical for gathering this information, enabling precise monitoring and control. Proprioception, in particular, can provide an estimation of the bending of the soft fingers, thus allowing for accurate pose estimation of the gripper.[3,4]

Since the great dexterity of soft grippers is related to the use of flexible and stretchable materials, soft sensors are crucial, as they do not alter the rigidity of the structure.[5,6] For effective proprioceptive soft robots, sensors should ideally combine mechanical compliance to avoid interfering with robot performance, compact dimensions to maintain a wide range of motion, high durability across thousands of deformation cycles, and resilience tailored to specific environments (e.g., from delicate surgical settings to harsh scenarios of rescue robots). Additionally, sensors should be easy to integrate and compatible with the robot's soft structure.[7] A promising strategy for successful soft grippers' bending proprioception involves integrating stretchable sensors within the structures to measure their bending angle. Different approaches can be adopted and frequently include optical sensors (optical fibers,[8] waveguides),[9] resistive sensors (liquid metals,[10] ionic liquids,[11] conductive yarns,[12] printed ionogels),[13] and piezoresistive sensors (nanocomposites,[14] textiles).[15] Other less-adopted solutions include capacitive sensors (nanocomposites,[16] textiles,[17]

G. De Luca, A. C. Bressi, R. Pathan, N. Pagliarani, M. Maselli, F. Greco, M. Cianchetti
The BioRobotics Institute
Scuola Superiore Sant'Anna
Viale Rinaldo Piaggio 34, 56025 Pontedera, Italy
E-mail: francesco.greco@santannapisa.it;
matteo.cianchetti@santannapisa.it

The ORCID identification number(s) for the author(s) of this article can be found under https://doi.org/10.1002/aisy.202401071.

DOI: 10.1002/aisy.202401071

G. De Luca, A. C. Bressi, R. Pathan, N. Pagliarani, M. Maselli, F. Greco, M. Cianchetti
Department of Excellence in Robotics and AI
Scuola Superiore Sant'Anna
Piazza Martiri della Libertà 33, 56127 Pisa, Italy

F. Greco
Interdisciplinary Center on Sustainability and Climate
Scuola Superiore Sant'Anna
Piazza Martiri della Libertà 33, 56127 Pisa, Italy

F. Greco
Institute of Solid State Physics
NAWI Graz, Graz University of Technology
Petersgasse 16, 8010 Graz, Austria

and ionic hydrogels),[18] magnetic sensors,[19] piezoelectric sensors,[15] and pneumatic sensors.[7,20,21] While the use of optical sensors to measure bending angles offers several advantages, such as high precision and sensitivity, a large working strain range, and the significant benefit of eliminating electronic components and wires in the sensitive active area, it also presents some challenges, such as the need for protection against physical damage, the complexity of integration, and high costs, further increased by the sophisticated supporting electronics for data acquisition.[22] Resistive sensors mostly exploit conductive liquids embedded in elastomers or stretchable conductive polymers and hydrogels. Despite fabrication challenges and leakage risks, conductive liquids offer significant potential for developing highly stretchable strain sensors, provided that design ensures reliable integration with solid conductors.[23] Piezoresistive sensors are usually based on elastomeric composites infused with conductive fillers, often have tunable mechanical and electrical properties, and are easy to fabricate. However, they can suffer from large hysteresis, nonlinearity, slow responses, and long recovery times. Typically, high filler concentrations are required to achieve good sensitivity, but they can increase the stiffness and thus interfere with the operation of the soft actuator.[24] Both resistive and piezoresistive elastomer-based sensors are suited for strain and bending measurements due to their flexibility, stretchability, and seamless integration with soft materials. Moreover, high deformations can be detected without altering the robots' mechanical properties.[25,26] Solutions embedding different conductive materials into flexible and stretchable polymers can maintain good performance under large deformation and may be tailored to sense the bending motion of soft robots.[24]

Within this context, laser-induced graphene (LIG) can be employed in innovative ways as the sensitive element in piezoresistive strain sensors for bending. LIG is created through laser-induced pyrolysis of carbon-rich materials into a 3D porous graphene structure. The laser scribing process is cost effective, easy, scalable, and does not require masks, chemicals, or solvents. LIG is commonly patterned onto synthetic high-performance polymer precursors, such as polyimide (PI), or onto some bioderived materials, such as wood, paper, and others.[27] The scribed LIG patterns can be transferred onto stretchable substrates[28,29] to widen the possible application fields: stretchable LIG composites can conform to complex surfaces and stretch without losing functionality. LIG's peculiar porous structure makes it very sensitive to strain and thus attractive for precise sensing in soft robotic applications. LIG-based strain sensors have been already investigated and have shown promising results.[21,28,30–32]

In this work, we investigate the integration of a thin, stretchable, low-cost, and easily fabricated sensor composed of LIG and dragon skin (LIG/DS) within pneumatic soft gripper fingers to assess bending performance. First, an in-depth investigation of the LIG/DS composite material, a comprehensive design analysis, and electromechanical quasistatic, dynamic, and fatigue characterizations are conducted on two different soft sensor designs made of LIG/DS. The optimal sensor design is then embedded into the fingers of a pneumatic soft gripper. Finite-element method (FEM) analysis identified the finger's neutral bending plane and four sensor positions are tested to validate the theoretical predictions of stress distribution and optimize sensor placement. The sensorized soft fingers are tested under static, dynamic, and fatigue conditions, to provide a comprehensive evaluation of their performance across diverse operating scenarios. Eventually, the calibration curve of the sensor is presented, demonstrating the potential of the LIG/DS sensor for accurate bending estimation, as it is needed during grasping tasks.

2. Results

This study aims to develop a sensor to provide proprioception to a finger-based pneumatic soft gripper through the sensorization of its fingers. The soft gripper consists of three flexible fingers, each designed as a pneumatic network (PneuNet) bending actuator with distinct top and bottom layers.[33] The upper layer comprises seven hollow chambers connected via a longitudinal channel. Upon applying positive pressure, the chambers inflate, causing the thinner longitudinal walls to expand and push onto each other. The thick bottom layer is inextensible but flexible and provides a mechanical constraint that promotes the structure's planar bending and forces the inward bending direction.[33] Starting from a bending angle $\theta = 0°$ at $P = 0$ bar, increasing the pressure results in a progressively larger θ angle (**Figure 1**A). The sensor, made of LIG and DS, is embedded within the bottom layer of the soft fingers. The choice of the DS matrix allows the sensor to be mechanically transparent, ensuring it does not alter the inherent mechanical properties of the soft actuator. The fabrication (Figure 1B) and characterization of the LIG/DS sensors are outlined in Section 2.1. The optimal sensor design is identified and embedded within the bottom layer of the soft fingers (Figure 1C) in various integration configurations to identify the most effective positioning, as detailed in Section 2.2.

2.1. Sensor

The mechanical characterization in tensile stress (Figure S1, Supporting Information) of the LIG/DS composite material resulted in Young's module of $E_{\mathrm{LIG/DS}} = 0.343 \pm 0.051$ MPa, to be compared with $E_{\mathrm{DS}} = 0.137 \pm 0.0005$ MPa found for a sample made of silicone elastomer only. Despite the increase, the two values are in the same order of magnitude, which confirms the initial hypothesis that embedding LIG in an elastomer matrix minimally modifies its stiffness, a crucial aspect for the realization of "transparent" sensors. Moreover, as illustrated in Section 4.4, the grippers are made of a thick layer of a slightly stiffer silicone (DS 30, $E_{\mathrm{DS30}} = 0.593$ Mpa without thinner)[34] with respect to the softer one (DS 10 Slow, $E_{\mathrm{DS10}} = 0.152$ MPa without thinner)[34] used for the sensor. Therefore the slight stiffness increase caused by LIG is overall compensated by this design choice.

Cross-sectional imaging of the LIG and LIG/DS samples (Figure S2, Supporting Information) reveals an average LIG thickness of ≈70 μm before peeling from the PI tape precursor (Figure S2A, Supporting Information) and ≈70 μm after peeling the LIG/DS (Figure S2B,C, Supporting Information).

Based on the Voigt model applied to our composite, the Young's modulus of LIG is estimated to be $E_{\mathrm{LIG}} = 4.428$ MPa. This value is significantly higher than the compressive moduli reported for LIG foams in the literature, which range from $E_{\mathrm{LIG}} = 40$ to $E_{\mathrm{LIG}} = 300$ kPa depending on the deformation

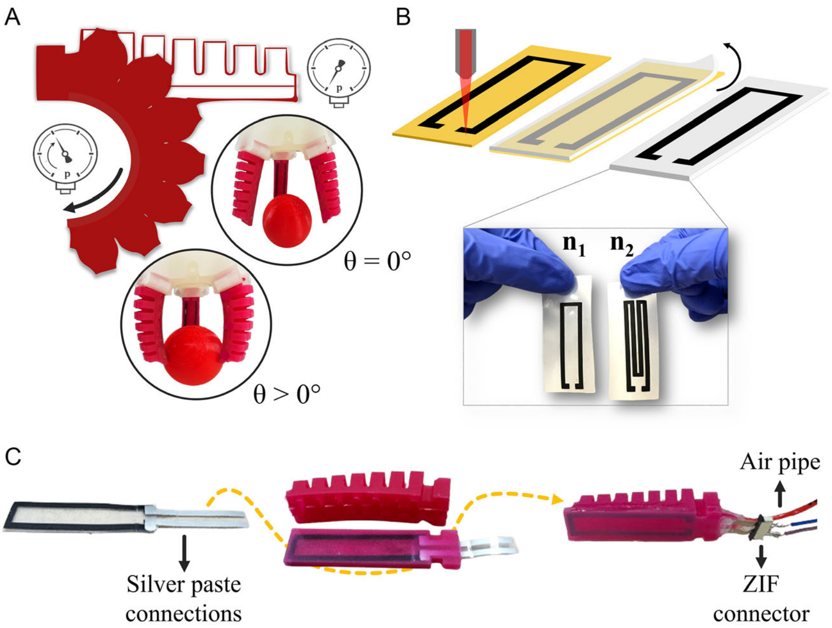

Figure 1. Conceptualization of the study. A) Graphics of the finger-based pneumatic soft gripper, with circular insets showing the rest condition ($\theta = 0°$) and the grasping of a spherical object ($\theta > 0°$). B) LIG/DS sensor fabrication: LIG tracks (n_1 and n_2 designs) are laser scribed on PI substrate; the DS precursor mixture is cast on top of the scribed PI and cured at 35 °C for 7 h; the DS with embedded LIG tracks is peeled from the PI. C) Soft finger fabrication and LIG/DS sensor integration in the finger: picture of n_1 LIG/DS sensor with electrical connections made of silver paste on a Mylar sheet; pictures of a top layer and a sensorized bottom layer of the soft finger; picture of a sensorized finger with electrical connections to the data acquisition system (ZIF connector) and air pipe.

phase.[35] This difference can be ascribed to the morphology and mechanical testing conditions: while the literature focuses on porous LIG foams under compression, our study investigates a denser, integrated LIG layer within a silicone matrix under tensile loading. However, the Voigt model's assumptions of homogeneity and efficient load transfer introduce some approximation, as LIG is a nonuniform porous structure, and its voids are filled with silicone. Hence, this estimation should be used with care.

An electromechanical characterization is carried out to quantify the piezoresistive behavior of LIG/DS sensors fabricated with two designs: a U-shape (n_1, resistance at rest before peeling $R_i \approx 0.7\ \text{k}\Omega$ and after peeling $R_0 \approx 4\ \text{k}\Omega$) and a serpentine shape (n_2, resistance at rest before peeling $R_i \approx 1.3\ \text{k}\Omega$ and after peeling $R_0 \approx 12\ \text{k}\Omega$). While before peeling $R_i(n_2) \approx 2R_i(n_1)$, in agreement with the difference in track lengths, for peeled-off tracks $R_0(n_2) \approx 3R_0(n_1)$. This discrepancy can be attributed to the manual nature of the peeling processing, during which the applied stresses may be distributed differently along the tracks. The observed change in resistance after peeling is in line with those reported for transfer to other substrates.[28] **Figure 2**A shows the results of both quasistatic and dynamic tensile tests. For both designs, the sensor response is mostly unaffected by varying the tensile strain rate, but the sensitivity of n_1 is always higher than that of n_2. While the operating range of n_1 is linear up to a strain of $\varepsilon = 30\%$, n_2 saturates after about $\varepsilon = 20\%$ (data after this strain values are omitted in the plot for clarity). Fatigue characterization (Figure 2B and Figure S3, Supporting Information) proves a stable performance after over 3000 cycles. An initial downward trend is observed, and an asymptotic stable value is reached for both n_1 and n_2. The transitory phase of ≈500 cycles corresponds to 12.7 ± 1.7 min. A 1 h pause is carried out at cycle 2000 to assess the performance stability after operation pauses. After the pause, a slightly increased sensor response is evidenced, but with a much shorter duration of the transitory phase, equal to 1.1 ± 0.7min; then the sensor response quickly returns to the same prepause asymptotic value. Considering the observed transitory behavior, we estimate the gauge factor (GF) when the asymptotic value is reached instead of calculating it on pristine sensors. The obtained results $\text{GF}_{n_1} = 87.5 \pm 1.83$ and $\text{GF}_{n_2} = 61.5 \pm 0.57$ highlight a higher sensitivity for n_1 design.

To investigate and rationalize the transitory phase behavior, the temperature of the sensor is assessed with a thermal IR camera during fatigue tests. A change in temperature (due to heat dissipation upon repeated cycling) could indeed in part explain that behavior. However, no significant change in temperature with time is observed (a representative sample of n_1 is reported in Video S1, Supporting Information).

Scanning electron microscopy (SEM) images of the exposed LIG surface in the LIG/DS sensors before and after a fatigue test (Figure 2C,D) show the evolution of the microstructure. The LIG part of the sensor shows a highly porous, sponge-like morphology, with a network of wrinkled graphene sheets intersecting at various angles, forming a 3D turbostratic structure. Cracks are present even in pristine samples (Figure 2C) and may have formed during the laser processing or the peeling process, which both induce stresses in the sample. The interface between LIG and silicone, crucial for sensor performance, appears to be strong

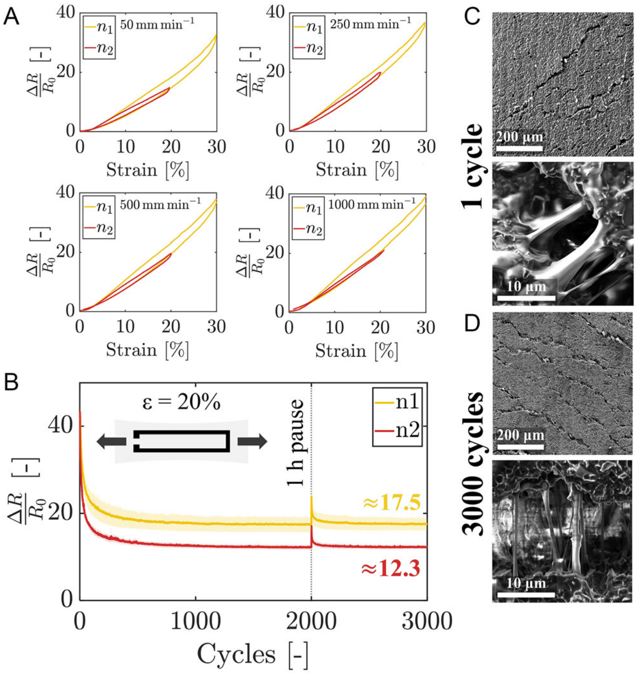

Figure 2. LIG/DS sensors characterization. A) Electromechanical quasi-static and dynamic characterization of n_1 (yellow) and n_2 (red) sensors. The cyclic tests were performed for five cycles from $\varepsilon = 0\%$ to $\varepsilon_{\max} = 30\%$ (for n_1) or $\varepsilon_{\max} = 20\%$ (for n_2) at four different speeds: 50 mm min^{-1} (yellow), 250 mm min^{-1} (orange), 500 mm min^{-1} (red), and 1000 mm min^{-1} (dark red). B) Electromechanical fatigue characterization of n_1 (yellow) and n_2 (red) sensors over 2000 cycles plus 1000 cycles after a 1 h pause. The cycles were performed from $\varepsilon = 0\%$ to $\varepsilon_{\max} = 20\%$, but only the maximum value for each cycle is reported for clarity. For each design, the maximum values are averaged over three samples. The standard deviation is depicted with a shaded area. SEM images of C) pristine (1 cycle) and D) fatigue-tested (3000 cycles) samples in stretched state at $\varepsilon = 20\%$. Two magnifications are reported here to gain an overview of the surface and a detail of the cracks.

and well distributed within the 3D structure of the sensors, indicating that the uncured silicone precursor mixture can penetrate and diffuse into the porous carbon structure during the fabrication. This is visible both on the LIG surface (with many silicone "bubbles" protruding from it, as highlighted in Figure 2C) and on the inside cracks (with many silicone "filaments" connecting LIG across cracks). After fatigue tests (Figure 2D), the samples show similar morphology, without significant modification in their microstructure. Slight differences are found at a larger scale: cracks formation is more widespread and the gaps within cracks are somehow increased. This likely causes the readjustment of conductive paths within the internal LIG network, with the damage reconstruction process gradually stabilizing after the prestretch of the sensor over multiple loading/unloading cycles.[36] Minor differences appear between different samples since the manufacturing process was manual and not entirely free of human errors; therefore, silicone more or less protruded through the LIG pores, and the cracks' density and orientation vary. However, all samples show a good LIG/DS interface even after fatigue tests, which is also reflected in their constant performances over time.

Since both designs show similar stability performances, a representative sample of n_1 is also tested up to 10 000 cycles and shows excellent behavior, confirming its suitability in long-term applications (Figure S4, Supporting Information). The sensor's capability to continuously monitor a constant state of strain (or bending, in its final application) was evaluated through static hold and release tests. Sensors with n_1 design demonstrated stable resistance readings under a static stretched condition over time (Figure S5, Supporting Information). The recorded signal-to-noise ratio (SNR) is 39.14 ± 0.31, indicating that the measurements were characterized by minimal noise. Despite the average delay to reach a stabilized signal condition being $t_d = 1.2 \pm 0.5$ s, the signal delay with respect to strain is in the order of ms, in line with what is reported in the literature.[2]

Overall the electromechanical testing results well align with the literature on LIG/elastomers strain sensors (**Table 1**). Most of the sensor designs investigated in other studies are based on line patterns of LIG, which was not a suitable solution in our case, namely the application within a soft robotic finger. In this case, the electrical connections of the two-terminal resistive

Table 1. Comprehensive comparison between LIG/elastomers sensors in literature and this work. For column "stability", the applied strain is indicated if different from $\varepsilon_{\max}$. Acronyms: KL: kraft lignin, PDMS: polydimethylsiloxane, PI: polyimide, PEEK: polyetheretherketone, EF: Ecoflex, DS: Dragon Skin, MC: microcracked, C: corrugated, S: serpentine, PSPI: photosensitive polyimide, MPU: medical polyurethane, U: U shape.

Materials	Design	GF	$\varepsilon_{\max}$ [%]	Stability [cycles]	Reference
KL-LIG/PDMS	line	20	60	5000	[57]
PI-LIG/PDMS	line	3.45	100	10 000 @50%	[58]
PI-LIG/PDMS	line	160	30	200	[59]
PI-LIG/PDMS	line	15.79	20	2000 @5%	[52]
PI-LIG/PDMS	line	2710.95	40	20 000	[37]
PI-LIG/PDMS	line	38	50	100 @10%	[60]
PI-LIG/PDMS	line	111.1	21	1500 @8%	[30]
PI + MoS$_2$-LIG/PDMS	line	1242	37.5	12 000 @4%	[38]
PEEK + PDMS-LIG[a]	line	78	53	1000 @10%	[61]
PI-LIG/silicone	line	132.5	80	1000 @50%	[62]
PI-LIG + Ag paste/EF	line	233.6	100	800 @80%	[39]
PI-LIG/EF	MC-line	191.55	50	1500 @20%	[36]
PI-LIG/EF	C-line	22.5	45	5000 @20%	[63]
PI-LIG/PDMS	4 ∥ lines	20 000	100	1000	[40]
PI-LIG/PDMS	square	86.5	110	100	[64]
PI-LIG/MPU	U	40	100	200 @30%	[28]
PEEK-LIG/PDMS	C-U	2203.5	6.8	15 000 @5%	[41]
PI-LIG/PDMS	S	37	70	1000 @20%	[65]
PI-LIG/PDMS + PSPI	S	35	110	10 000 @90%	[66]
PI-LIG/DS sponge	S	1.3	60	1000 @40%	[67]
Paper + wax-LIG/MPU	S	128.9	10%	3600	[68]
PI-LIG/DS	U	87.5	30	10 000 @20%	this work
PI-LIG/DS	S	61.5	20	10 000 @20%	this work

[a] not transferred.

device should be both on the same side (wrist). Our sensors show great stability over time, reaching 10 000 cycles without modifying their performances. Due to the stability of the signal at the end of the test, it is fair to assume that they would last even longer. It should be also noted that our investigation focused only on the $\varepsilon = 0$–30% range, necessary for our soft robotic application. However, since the resistance trend of the n_1 design is still linear at the maximum tested strain, the sensor can possibly work well even at higher strains. Two additional considerations should be made regarding the GF values. First, no study so far reported an assessment of GF after the prestretch of the sensor, which represents the steady-state behavior. Studies rather focused on the immediate response of the sensor, without taking into account any adjustments over multiple cycles. In the case of the present study, instead, we deemed that the GF value reported is more representative of the real, long-term performance, despite being significantly lower than the value obtainable considering just the response of the first cycles ($\text{GF} \approx 200$, as inferrable from Figure 2B). Second, when extremely high GF values ($\text{GF} > 200$) are reported in other studies, they may not represent accurately the actual GF of the sensors, since they are the highest values among multilinear working regions, often at high strains.[37–40] All these studies, indeed, demonstrate GF values in the same order of magnitude of our sensors in the first linear working region. Only Li et al.[41] outperform the state of the art, showing excellent strain sensitivity also at very low strain values during tests before integration. The extreme sensitivity of that sensor however backfires during operations with the soft grippers, since even the inflation pressure influences the reading of the sensor, and numerous flicks appear due to the elastomer resilience (as also discussed in Section 2.2).

Eventually, due to the wider working strain range, higher GF, shorter scribing times, and easier peeling process, n_1 design is selected over n_2 as the final design for the integration in the fingers of the pneumatic soft gripper.

2.2. Finger

The FEM analysis of x-directional stress in the soft bending actuator under full bending conditions with an applied pressure of 0.6 bar is reported in **Figure 3**. The objective of this analysis is to estimate the location of the neutral bending plane, which is crucial for understanding the stress distribution and optimizing the sensor placement. The image shows the x-directional stress distribution across seven different cross-sectional surfaces of the actuator, taken at intervals of 0.5 mm, starting from the lower part of the bottom layer and going toward the junction separating the bottom layer and the inflatable chambers. Each subimage indicates the mean x-directional stress distribution (M) at the respective cross section. At the cross section of $z = 3$ mm, the mean stress is $M = +0.100$ MPa, showing higher positive values and indicating tensile stress on the outer layers of the actuator. At $z = 2.5$ mm, the mean stress is $M = +0.070$ MPa, with the tensile stress still significant but slightly reduced. At $z = 2$ mm, the mean stress is $M = +0.020$ MPa, bringing the stress values closer to 0, indicating proximity to the neutral plane. Another measurement at $z = 1.5$ mm shows a mean stress of $M = +0.007$ MPa, suggesting it is very close to the neutral

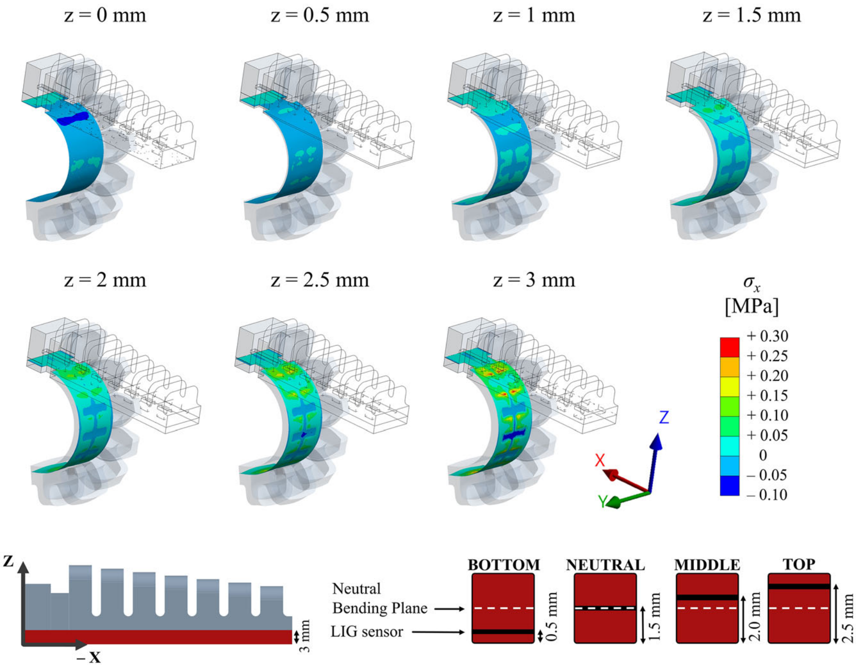

Figure 3. FEM analysis of the fingers of the pneumatic soft gripper. X-directional stresses are shown at different cross sections z of the bottom layer of the finger. On the bottom of the figure, a side-view graphic of the soft finger (left) highlights the thickness of the bottom layer (dark red), and the cross-section graphics of the bottom layer show the LIG/DS sensor positions chosen for the investigations (right), which undergo compressive (bottom configuration), null (neutral configuration), and tensile (middle and top configurations) stresses.

bending plane. At $z = 1$ mm, the mean stress turns negative and is $M = -0.001$ MPa, indicating the start of compressive stress. Further measurements at $z = 0.5$ and $z = 0$ mm show mean stresses of $M = -0.007$ and $M = -0.008$ MPa, respectively, indicating increasing compressive stress. Thus, the neutral bending plane is estimated to lie within the interval between $z = 1.5$ and $z = 1$ mm, where the mean x-directional stress shifts from slight tensile to slight compressive values, approaching 0 MPa with a numerical error of less than 10^{-2}. This range reflects the transition zone, where stress values gradually decrease toward zero before becoming negative. This interval-based estimate reflects the semiquantitative method used in the analysis, with stress values measured at discrete cross-sectional intervals of 0.5 mm. This resolution not only ensures a good level of accuracy in identifying the transition zone but also aligns with the precision achievable in sensor placement during the manual fabrication process using casting molding. Studying the detailed stress distribution across different cross-sections helps in understanding the actuator's mechanical behavior under bending conditions by identifying the neutral plane position. This, in turn, is used for the correct positioning of the sensor to ensure the sensor's best performance, in terms of linearity and reliability.

Based on the FEM analysis results, and in order to validate them experimentally, the finger characterization described in Section 4.6 is carried out for four different sensor positions within the finger bottom layer. The first position is BOTTOM, which is below the neutral bending plane ($z_{\text{bottom}} = 0.5$ mm): a location where the sensor should be subjected to compressive stress. The second is NEUTRAL, which is approximately on the predicted neutral bending plane ($z_{\text{NAUTRAL}} = 1.5$ mm). The third and fourth are MIDDLE and TOP, located, respectively, at 0.5 and 1.0 mm above the neutral plane ($z_{\text{MIDDLE}} = 2.0$ mm and $z_{\text{TOP}} = 2.5$ mm): locations where the sensor should be subjected to tensile stress. The maximum strain for each of the four sensor integration configurations $\varepsilon_{\text{CONF}}$ is evaluated as described in Equation (8), yielding: $\varepsilon_{\text{BOTTOM}} = -4.7\%$, $\varepsilon_{\text{NEUTRAL}} = 0.7\%$, $\varepsilon_{\text{IDDLEM}} = 4.1\%$, and $\varepsilon_{\text{TOP}} = -9.1\%$ $\varepsilon_{\text{TOP}} = -9.1\%$ (Figure S6, Supporting Information). These results further corroborate the position of the neutral bending plane, where strain due to bending is theoretically null. Considering the inherent inextensibility of the bottom layer of the soft finger and the consequent absence of a stretch of the structure as a whole during inflation,[33] the near-zero (but still positive) strain at z_{NEUTRAL} confirms that this plane undergoes an almost negligible elongation and therefore the neutral bending plane lies indeed within the interval $Z = 1.5$ to $Z = 1$ mm.

The electromechanical static characterization of sensors placed in the four different positions (**Figure 4** and Figure S7, Supporting Information) is in good agreement with predictions of the FEM analysis and confirms the predicted stress distribution. Samples in BOTTOM configuration indeed undergo compression stresses, as evidenced by the negative resistance change with increasing bending angle evidenced in Figure 4C. Sensors placed at BOTTOM location have good linearity but only for $\theta < 60°$ and a maximum hysteresis percentage error of $H_{\text{max\%}}$. Samples in TOP and MIDDLE locations undergo tensile stresses, with increasing resistance with the increase of the bending angle. TOP is characterized by a linear response up to $\theta = 80°$. The loss of linearity and flattening of the trend for $\theta > 80°$ may be due to the pressure applied by the air chambers on the sensing layer, with a consequent decrease in resistance. TOP location is the closest to the inflatable chambers and thus more prone to this effect with respect to others. In this configuration, the maximum hysteresis percentage error is $H_{\text{max\%}} = 45\%$. Sensors placed in MIDDLE location maintain good linearity throughout the whole bending angle range. Its maximum hysteresis percentage error is significantly lower than TOP, with only $H_{\text{max\%}} = 8\%$. The samples in NEUTRAL configuration further confirm the theoretical location of the neutral bending plane since the sensor reading shows evident instabilities, indicating a mix of small tensile

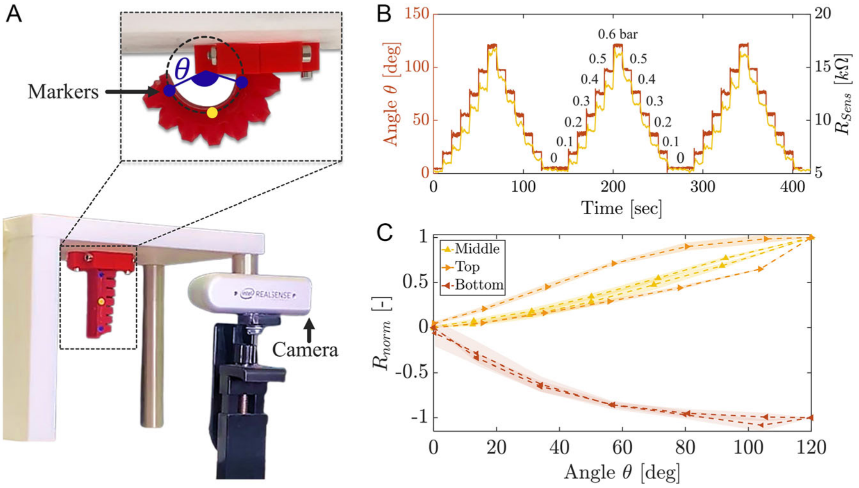

Figure 4. Electromechanical static characterization of the soft pneumatic finger for the different positioning of the LIG/DS sensor. A) Test setup for sensorized finger characterization; the inset shows the evaluation of the bending angle θ. B) A representative test protocol (three cycles of stepwise increase/decrease of input pressure 0–0.6 bar) with measured bending angle θ (y-left) and sensor resistance R_{sens} (y-right) over time for the sensor placed in MIDDLE location. The bending angle linearly increases with the pressure.[53] C) Trends of normalized resistance R_{norm} over bending angle θ for sensors placed in TOP, MIDDLE, and BOTTOM integration configurations.

and compression stresses acting on the sensor (Figure S7B, Supporting Information). Moreover, the resistance variation over the cycles with respect to the initial value is much smaller than the other integration configurations, confirming FEM predictions.

The electromechanical dynamic characterization of sensorized fingers (Video S2, Supporting Information, **Figure** 5A,B,C and Figure S7C, Supporting Information) shows superimposing curves at different angular rates for each integration configuration. This demonstrates that the sensor response is independent of the angular rate and the trend behavior is similar to the curves of the static characterization (Figure 4C). Overall, the results of static and dynamic tests are in good mutual agreement for linearity and hysteresis and align well with predictions from FEM analysis in terms of stress modes. Based on these results, it is concluded that MIDDLE is the best integration configuration and is therefore adopted for further investigations.

The electromechanical dynamic fatigue characterization on MIDDLE samples (Figure 5D) highlights a constant asymptotic behavior of the sensor throughout the whole 150-cycle plus 150-cycle after a 20 min pause test, with a transitory of 70 cycles, ≈6 min. Good repeatability in the amplitude of the cycles is observed before and after the pause. This result solves the minor problem related to the small discrepancies after operation pauses of the sensor alone.

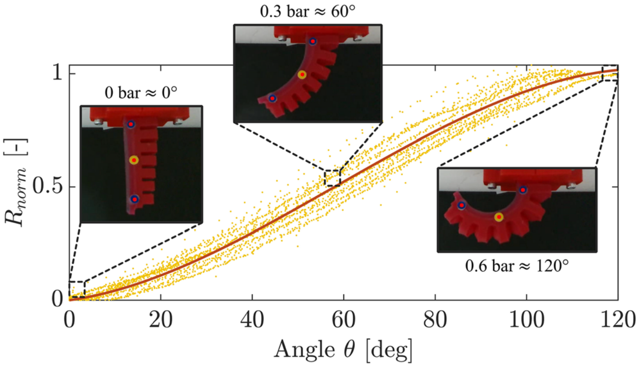

Figure 6. Calibration curve for LIG/DS sensors (n_1 design) embedded in the fingers of a pneumatic soft gripper (MIDDLE integration configuration), obtained from the data of electromechanical static and dynamic tests of three finger samples. The insets show pictures of one representative sensorized finger at $P = 0$ bar, $P = 0.3$ bar, and $P_{max} = 0.6$ bar, which correspond to a bending angle of $\theta \approx 0°$, $\theta \approx 60°$, and $\theta \approx 120°$, respectively.

A calibration curve for MIDDLE sensor integration configuration was realized using a third-degree polynomial function C(x) to fit the cumulative data from static and dynamic tests (**Figure 6**). The function is reported in Equation (1), where $a_1 = -8.48 \cdot 10^{-7}$, $a_2 = 1.47 \cdot 10^{-4}$, $a_3 = 2.86 \cdot 10^{-3}$, $a_4 = 0$.

$$C(x) = a_1x^3 + a_2x^2 + a_3x + a_4 \tag{1}$$

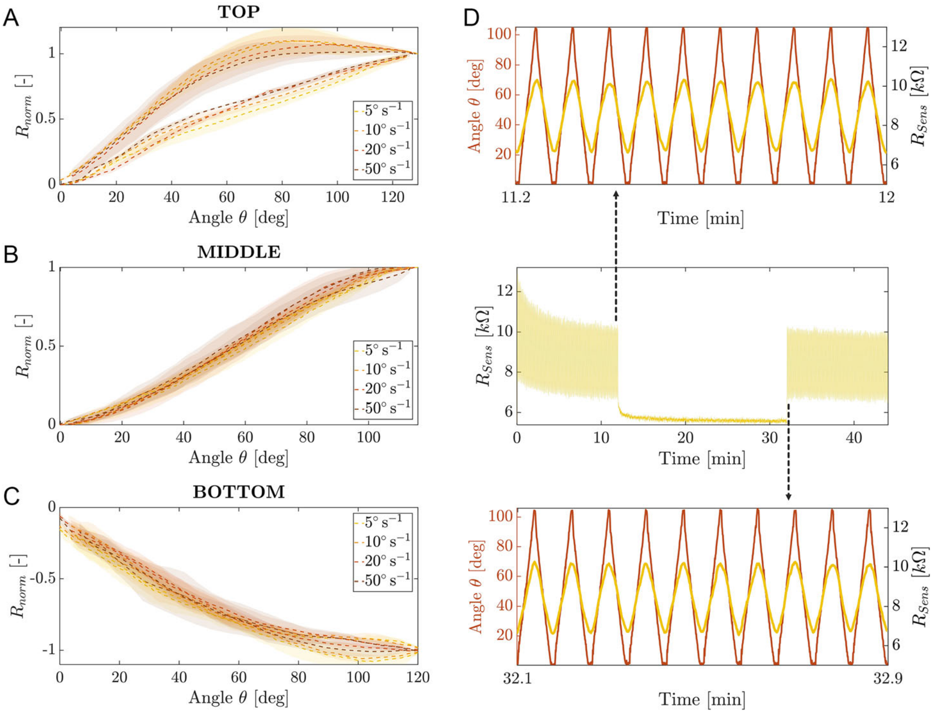

Figure 5. Electromechanical dynamic characterization of the sensorized soft pneumatic finger: trend of normalized resistance R_{norm} versus bending angle θ for A) TOP, B) MIDDLE, and C) BOTTOM sensor integration configurations. The cyclic tests were performed for five cycles at four different speeds: 5° s^{-1} (yellow), 10° s^{-1} (orange), 20° s^{-1} (red), and 50° s^{-1} (dark red). The average value over three samples is represented with a dashed line, the standard deviation with a shaded area with the same color. D) Fatigue characterization of MIDDLE sensor resistance for consecutive pneumatic actuation cycles of the soft finger (0–0.6 bar) over 150 cycles, plus other 150 cycles after a 20 min pause. The insets show the measured angle and resistance values during the ten cycles immediately before (top) and after (bottom) the pause.

Table 2. Comprehensive comparison between different sensors for soft grippers in literature and this work. Acronyms: R: resistive, CL: conductive liquid, U: U-shaped sensor, eGaIn: eutectic Gallium-Indium, RS: rectangular-shaped sensor, n.a.: not available, 3D-P: 3D-printed, PPSS: PEDOT: PSS, CTPU: conductive polyurethane, PVA: polyvinyl alcohol, P: piezoresistive, FL: full sensing layer, CLIG: corrugated LIG, LIG: laser-induced graphene.

Class	Materials	Design	GF	$\varepsilon_{\max}$ [%]	Range [°]	Position	Reference
R	CL (NaCl water)	U	n.a.	n.a.	0–120	Bottom	[11]
R	CL (eGaIn)	RS	n.a.	n.a.	0–211[a)]	Top	[44]
R	3D-P CTPU	U	n.a.	5[b)]	0–172[a)]	Bottom	[45]
R	3D-P PPSS + PVA	U	4.07	300	0–38[a)]	Top	[46]
R	SP Ag ink	U	5.759	2[b)]	0–150[a)]	+0.675 mm[c)]	[47]
P	Carbon fibers	FL	n.a.	10	0–120	Bottom	[48]
P	CLIG	U	2203.5	6.8	0–120	Bottom	[41]
P	LIG	U	87.5	30	0–120	+0.5 mm[c)]	this work

[a)] inferred from the data reported in the original work. [b)] considering only the linear region. [c)] considering the neutral bending plane position as 0 mm.

The coefficient a_1 is negative, meaning that for high-angle values the resistance increase decelerates, suggesting a sort of saturation effect of the resistance. The coefficient a_2 indicates the change in curvature for the intermediate-angle values. The small value proves the linearity of the curve, with a small bending upward for middle-angle values. The coefficient a_3 refers to the steepness of the curve itself, indicating a proportional positive relation between resistance and angle. The coefficient a_4 is null because of the imposed constraints in the fitting. Overall, the behavior of the sensor is linear in the range from $\varepsilon = 5$ to $\varepsilon = 110°$, with a smaller sensitivity for higher angles, allowing for unique bending angle determination. For this reason, n_1 sensor in MIDDLE configuration can be considered an excellent alternative to more common solutions for the measurement of proprioception in our soft gripper.

Indeed, compared to optical sensors,[42,43] the fabrication and integration process of our sensor is significantly easier and allows for greater flexibility in design and adaptability. An interesting comparison of our sensorized soft gripper with the state-of-the-art resistive and piezoresistive sensors for proprioception estimation in soft fingers is reported in **Table 2**. For what concerns resistive sensors, while the use of conductive liquids[11,44] presents a more complex fabrication process, the 3D-printed[45,46] and screen-printed[47] tracks provide significant flexibility in the sensor's design, low cost, and easy processing, similar to LIG-based sensor fabrication. Despite these advantages, resistive sensors show a narrower linear response range and/or lower GF with respect to our LIG/DS sensors. Indeed, Dezaki et al.[45] showed a linear response range of only up to $\varepsilon = 5\%$, even though their operational range extended to $\varepsilon = 300\%$. Shen et al.[46] instead, proved a high stretchability up to $\varepsilon = 300\%$, but with a significantly lower GF = 4.07. Moreover, the characterization of the soft finger is carried out only up to ≈38°. Also, Koivikko et al.[47] highlighted some drawbacks, such as a limited linear response range (only $\varepsilon < 2\%$) and a low GF = 5.759. Additionally, none of these studies investigate the optimal sensor positioning for response efficacy, resulting in the sensor being placed either at the bottom or top position. Only Koivikko et al.[47] placed the sensor in a specific position within the structure, at 675 μm over the neutral plane, yet no explanation is provided for this choice.

When considering piezoresistive sensors, Pan et al.[48] used carbon fibers-based piezoresistive composites to create the bottom conductive layer of a pneumatic soft finger actuator. The authors report that the sensor did not influence the flexibility of the actuator for deformations but only for $\varepsilon < 10\%$. In contrast, our sensor features Young's modulus that ensures minimal impact on flexibility, allowing the actuator to maintain its performance and adaptability under higher strain conditions. Li et al.[41] show a proof of concept of a similar LIG-based strain sensor for the sensorization of a soft finger. The LIG structure differs since they use a corrugated LIG to realize the conductive tracks. Compared with our sensor, it shows a narrower working range, with an $\varepsilon_{\max} = 608\%$, but a higher GF = 2203.5 in the strain range ε from 5% to 6.8%. However, the mechanical influence of the sensor attached to the original soft finger is not addressed but may be relevant. Moreover, also in Li et al.[41] no analysis of the optimal position of the sensor is carried out, resulting in an arbitrary placement of the sensor on the bottom side of the finger. This position exposes the sensor to compressive stresses, potentially reducing its sensitivity.

3. Conclusion

Our study presents a novel, reliable, and high-performance method for bending angle proprioception in a finger-based pneumatic soft gripper, using a sensor made of LIG and DS, a commercially available silicone widely employed in soft robotics. The sensors' materials and design have been selected to avoid altering the original flexibility of the soft gripper, which is designed to handle delicate objects, such as fruits, vegetables, glassware, or soft materials in general. To optimize sensor design, we evaluated a U-shaped (n_1) and a serpentine-shaped (n_1) configuration, finding that the U-shaped (n_1) design provided superior performance with a steady-state GF of $\mathrm{GF}_{n_1} = 87.5 \pm 1.83$ and a linear response up to a strain of $\varepsilon = 30\%$ and durability of at least 10 000 cycles. Additionally, FEM analysis is conducted to locate the neutral bending plane, found at approximately $\varepsilon_{\mathrm{NEUTRAL}} = 1.5\%$ mm from the finger's bottom layer. Experimental validation confirmed this position through a comprehensive assessment of the sensor's performance at four different locations (TOP, MIDDLE, NEUTRAL, and BOTTOM). This study helped to identify the optimal sensor placement: the MIDDLE configuration provided the best performance, with a linear response of the sensor up to $\theta = 110°$ and a low maximum hysteresis error of 8%. The sensorized fingers were tested for 300 cycles and showed good repeatability in the amplitude of cycles at the steady state, even across an operation pause. Eventually, we obtained the calibration curve, defining a consistent relationship between the bending angle and resistance variation, enabling precise monitoring of finger movements during grasping tasks.

This investigation lays the foundation for further research on this promising LIG sensor solution for soft fingers. Future work should focus on using proprioception to control the fingers' bending angle and explore the possibility of measuring other physical parameters—such as twisting strain, pressure, contact interactions, and temperature changes—that have previously been studied with LIG sensors in other contexts.[28,49] This approach could enable the development of fully closed-loop controlled soft robotic systems, expanding their functional range and precision. In addition, due to the flexibility and cost-effectiveness of the fabrication process, the ease of integration, and the low invasiveness of the LIG/DS sensor, its design could be tailored to other soft robots and also in different fields, such as prosthetics and rehabilitation, in which the flexible sensor can provide minimal interference with natural human movement while enabling responsive, real-time monitoring.

4. Experimental Section

Sensor Design and Fabrication: A CO_2 laser cutter (Universal Laser Systems VLS 3.50, laser wavelength 10.6 μm, $P_{\max} = 50$ W) equipped with a 2.0 beam collimator (nominal beam size: 130 μm) was used to create LIG patterns on PI tape (MS Lehner Kapton 1901 from Dupont, thickness = 50 μm). The laser scribing for LIG fabrication was conducted in ambient conditions, with the tape attached to plexiglass support. The laser cutter was operated in raster mode, with laser settings: power $P = 10\%$, speed $S = 10\%$, points per inch PPI = 500, image density ID = 5 (defining a spacing between consecutive rastered lines of 280 μm), and operating in focused conditions on the PI surface. A commercially available liquid silicone precursor DS 10 Slow (Smooth-On) was manually mixed with Silicone Thinner (Smooth-On) in a 1:100 w w^{-1} ratio. The mixture was cast on top of LIG tracks, evenly spread with a manual film applicator (ZUA 2000, Zehntner) at a thickness of 0.8 mm for dogbone samples and 0.5 mm for sensor samples. This allowed the liquid elastomer DS mixture to infiltrate the porous LIG structure before curing in an oven at 35 °C for 7 h. The resulting cured LIG/DS composite was then peeled from the PI substrate. For sensors fabrication, two different LIG patterns were scribed n_1, n_2 displayed in Figure S8, Supporting Information.

LIG Characterization: Microstructure and Morphology: LIG morphology was investigated with a Hirox HR 5000 (E) digital optical microscope equipped with a high-range motorized triple zoom lens and with a Phenom XL SEM (ThermoFisher Scientific). Samples for surface morphology investigation were obtained by cutting a 20 × 20 mm portion of the sensors with a fine blade. Samples for cross-section morphology were obtained with cold fragile fracture by immersion in liquid nitrogen for 30 s and subsequent bending with tweezers to break them.

LIG Characterization: Mechanical Characterization: An Instron 5965 series universal testing machine (Instron Corp, Canton, MA) equipped with a 10 N load cell was employed for mechanical properties assessment, coherently with ASTM D882 standards. Dogbone samples of DS and LIG/DS (with LIG covering the entire dogbone surface) were used for uniaxial tensile tests. The testing protocol included ten blocks with increasing maximum strains $\varepsilon_{\max}$ from 0% to 100%, each comprising five consecutive cycles and a pause of 20 s at the end. The elongation rate was 50 mm min^{-1}. The Young's modulus E was evaluated on the first 10% of strain. For silicone samples, a thickness $t_s = 800$ μm was considered. For LIG/DS samples, a silicone thickness $t_s = 800$ μm and a LIG thickness $t_{\mathrm{LIG}} = 40$ μm (taken from Figure S2, Supporting Information) were considered as a plausible approximation despite part of the LIG being embedded within the thickness of the silicone. LIG Young's modulus E_{LIG} was obtained through the Voigt model,[50] as reported in Equation (2), where ν_s is the volume fraction of silicone, with the hypothesis of the same in-plane area since the LIG covered the whole surface of the dogbone samples (Figure S1C, Supporting Information).

$$\begin{aligned} \nu_s &= \frac{t_s}{t_s + t_{\mathrm{LIG}}} \\ E &= E_s \nu_s + E_{\mathrm{LIG}}(1 - \nu_s) \end{aligned} \tag{2}$$

Sensor Characterization: The LIG sensors were characterized by electromechanical tests. An Instron 5965 series universal testing machine (Instron Corp, Canton, MA) equipped with a 10 N load cell was employed in uniaxial tensile tests to apply a controlled strain for quasistatic, dynamic, and fatigue tests. The sensors' resistance was acquired through a voltage divider circuit ($R = 200$ kΩ) using a data acquisition board (National Instrument, DAQ USB-6009) and a custom LabVIEW interface. The output tension (V_{out}) of the circuit and the corresponding sensors' resistance values were calculated as shown in Equation (3), where the input tension was $V_m = 5$ V and the resistance of the voltage divider was $R = 200$ kΩ.

$$R_{\mathrm{sens}} = R \cdot \frac{V_{\mathrm{out}}}{V_{\mathrm{in}} - V_{\mathrm{out}}} \tag{3}$$

A visual representation of the setup is reported in Figure S9, Supporting Information. The data were processed and analyzed with MATLAB (MathWorks Inc., Natick, MA, USA).

Sensor Characterization: Electromechanical Quasi-Static Characterization: The testing protocol consisted of five consecutive cycles with strain from $\varepsilon = 0$ to $\varepsilon_{\max} = 30\%$. Four different samples were tested for each design (n_1 and n_2). The elongation rate was 50 mm min^{-1} to perform a quasistatic measurement. The results were postprocessed by removing the first cycle of each sensor and normalizing $\Delta R = R_{\mathrm{sens}} - R_0$ (where R_0 was the first acquired value, in rest position) over R_0.

A hold-and-release test was performed on three samples for n_1 design, to confirm the stability of the sensor signal in static stretched conditions. The samples were first stretched to $\varepsilon_{\max} = 20\%$, held at $\varepsilon_{\max}$ for 600 s, then released to $\varepsilon = 0\%$, and held for 600 s. The elongation rate was 50 mm min^{-1}. SNR was evaluated according to Equation (4),[51] where $R_{\mathrm{sens\_mean}}$ was the average of the R_{sens} values obtained once the steady-state condition was reached, excluding the first and last 30 s.

$$\mathrm{SNR} = 20 \log_{10}\left(\frac{R_{\mathrm{sens\_mean}}}{\mathrm{std}(R_{\mathrm{sens\_mean}})}\right) \tag{4}$$

Delays to reach a stabilized signal condition of the sensors (t_d) were evaluated as reported in Equation (5),[52] where t_s was the stretching time from $\varepsilon = 0\%$ to $\varepsilon = 20\%$, and t_r was the response time of the sensor, evaluated from the starting stretching time until R_{sens} reached the $R_{\mathrm{sens\_mean}}$, with an error of 5%.

$$t_d = t_s - t_r \tag{5}$$

Sensor Characterization: Electromechanical Dynamic Characterization: Four samples for each design were tested at three different elongation rates (250, 500, and 1000 mm min^{-1}). The testing protocol included six blocks with increasing strains from 0% to 30%, each comprising five consecutive loading/unloading cycles and a pause of 20 s at the end. The results were postprocessed removing the first cycle of each block and normalizing $\Delta R = R_{\text{sens}} - R_0$ (where R_0 was the first acquired value, in rest position) over R_0.

Sensor Characterization: Electromechanical Fatigue Characterization: Three samples for each design were tested at the maximum strain at which both showed a stable behavior $\varepsilon_{\max} = 20\%$, for 2000 cycles, plus 1000 cycles after a 1 h pause. The elongation rate was $1000\,\text{mm min}^{-1}$. Once signal stabilization was achieved, the GF was calculated as reported in Equation (6), where $\Delta R = R_{\text{sens}} - R_0$ is the resistance variation.

$$\text{GF} = \frac{\Delta R / R_0}{\varepsilon} \tag{6}$$

A thermal IR camera (A700 Pro SC Kit, Flir) was used to evaluate the temperature of the samples during the fatigue tests to identify any thermal energy dissipation.

One sample for n_1 design was also tested at $\varepsilon_{\max} = 20\%$ for 10 000 cycles at an elongation rate of $1000\,\text{mm min}^{-1}$.

Finger Fabrication and Sensor Integration: The soft finger presented was a pneumatic network (Pneunet) bending actuator made of a top and a bottom layer, with a specific design based on previous works.[53] The fabrication of the finger consisted of a multistep open molding procedure. The molds were designed using SolidWorks and 3D printed using a ProJet MJP 3600 from 3D Systems. Both layers were produced with a commercially available elastomer DS 30 (Smooth-On) with a 1:100 Silicone Thinner (Smooth-On) and red dye (Smooth-on, Silc Pig PMS 186C), cast into the molds, degassed, and cured in the oven at 35 °C for 7 h.

The sensor was integrated during the manufacturing of the bottom layer, at different heights (see Section 4.5). Before integration, the sensor's electrical contacts were obtained with screen-printable stretchable silver paste (CI1036, Nagase ChemteX) spread with a single-use mask on a biaxially oriented polyethylene terephthalate sheet (Mylar RS PRO, thickness = 23 μm). After removing the mask, the silver paste tracks were aligned with the LIG and cured in the oven at 120 °C for 15 min to obtain a strong interface. The excess material was then removed for proper fitting of the sensor in the bottom layer mold.

After curing, the top and bottom layers were demolded and joined using the same silicone, with the insertion of the pipe for the air between them.

The electrical connections emerging from the finger were plugged into a ZIF connector (MOLEX 52 271-1079) and connected to the same acquisition system used for the electromechanical tests.

FEM: To position the sensor within the soft robotic finger, an FEM analysis was employed. This analysis involved estimating the location of the neutral bending plane, which was the plane within the finger where no longitudinal strain occurred during bending.[54] The model was developed with the Static Structural Analysis tool of ANSYS Workbench using the real finger dimensions reported in Pagliarani et al.[53] The material used to manufacture the finger was DS 30-A silicone rubber. In the simulation, it was virtualized using a 3rd-order Yeoh model for hyperelastic, incompressible materials with the strain energy function U reported in Equation (7), where C_i were the material coefficients and I_1 was the first strain invariant.

$$U = \textstyle\sum_{i=1}^{3} C_i (I_1 - 3)^i \tag{7}$$

The coefficients were identified by fitting the model to the experimental data obtained through standard uniaxial tensile tests (ASTM D142) at a rate of $200\,\text{mm min}^{-1}$ and resulted in $C_1 = 0.01039$, $C_2 = -0.00037$, and $C_3 = 0.00011$ MPa. As boundary conditions, the finger was fixed at one end, pressure was applied on the inner walls to simulate the air input, and the effect of the standard earth gravity was considered. When inflated, a soft bending actuator demonstrated planar movement, resulting in a nontrivial distribution of longitudinal stresses. Unlike a linear structure, such as a beam where the neutral bending plane is centrally located, the stress distribution in a soft bending actuator is more complex and requires detailed analysis. When positive pressure is applied, the soft bending actuator bends around the *y*-axis. To determine the neutral bending plane, the *x*-axis directional stress was evaluated under full bending conditions at an input pressure of 0.6 bar. This estimation involved analyzing the *x*-axis directional stress across seven surfaces that sampled the bottom layer of the soft finger at 0.5 mm intervals. For each surface, the mean *x*-axis directional stress was calculated for each interchamber distance, ignoring the stress concentrations caused by the pressurization of individual chambers. The neutral plane was identified as the surface where the mean *x*-axis directional stress was closest to 0 MPa, with a numerical error margin of less than 10^{-2}.

The arc length was estimated by sampling ten discrete points along the curvature of the soft finger across seven surfaces that sampled the bottom layer at 0.5 mm intervals. The total arc length was computed by summing the distances between consecutive points. This analysis was conducted on the rest ($P = 0$ bar) and bent conditions ($P_{\max} = 0.6$ bar). The maximum strain related to each of the four integration configurations $\varepsilon_{\text{CONF}}$ of the sensor was evaluated as reported in Equation (8), where L_0 was the length of the bottom layer of the finger in rest conditions.

$$\varepsilon_{\text{CONF}} = \frac{L_{\text{CONF}}(P_{\max} = 0.6\ \text{bar}) - L_0}{L_0} \cdot 100 \tag{8}$$

Finger Characterization: An experimental framework was devised to assess the sensor's capability in estimating bending angles, aiming to accurately model the correlation between the finger's bending angle and the sensor's voltage output. The setup comprised several components: a pneumatic source connected to a proportional pneumatic regulator (Festo, VEAB-L-26-D7-Q4-V1-1R1) to control air pressure inside the actuator chambers; a 3D-printed clamp to mount the actuator to the rigid platform; a data acquisition board (National Instrument, DAQ USB-6009) for transmitting pressure commands to the actuator and collecting voltage signals from the sensor during actuation cycles, through a voltage divider circuit ($R = 200\,\text{k}\Omega$) and a custom LabVIEW interface; and a camera (RealSense, 1920 × 1080 resolution, 30 fps) to capture the finger's bending angle in real time. To analyze the camera data and derive bending angle information, three colored markers (5 mm in diameter) were positioned at equal intervals along the actuator's length in correspondence to the first, fourth, and seventh air chambers, similar to what was outlined in Ji et al.[55] HSV color threshold was employed to isolate the marker region contours, with each region's center point identified as coordinates. These three points were then used to calculate the central angle of the arc formed by the markers, thereby determining the current bending angle.

The capture script was designed as a periodic task operating at a frequency of 30 Hz. Its primary function was to monitor the actuator while isolating the three markers through masking. The center point of each marker was calculated based on the corresponding pixels. A constant curvature model was employed,[56] and the bending angle was defined as the central angle θ between the endpoints. This was achieved by calculating the angle between the two vectors that connected the three markers defined as α (as shown in Figure S10, Supporting Information), where $l_1 = l_2 = l$, and converting it with the relationship demonstrated in Equation 9, where the angle α was found as shown in Equation 10.

$$\begin{aligned} \varphi &= \frac{180 - \alpha}{2} \\ 180 &= 90 + \varphi + \frac{\theta}{4} \\ \theta &= 2\alpha \end{aligned} \tag{9}$$

$$\alpha = \arccos\left(\frac{l_1 \cdot l_2}{|l_1||l_2|}\right) \tag{10}$$

The constant curvature assumption was employed, as the error between the shape given by theoretical predictions and the results were found to be negligible (see Supporting Information and Figure S11, Supporting Information).

The fingers were tested from $P = 0$ bar to $P_{max} = 0.6$ bar, which corresponded to approximately a bending angle of $\theta = 120°$, suitable to grasp different objects, as reported in the literature (Table 2).

The results were postprocessed normalizing $\Delta R = R_{sens} - R_0$ (where R_0 was the first acquired value, in rest position) with respect to the absolute ΔR value calculated at $P_{max} = 0.6$ bar as reported in Equation (11).

$$R_{norm} = \frac{\Delta R}{|\Delta R(P_{max} = 0.6\ \text{bar})|} \tag{11}$$

Finger Characterization: Electromechanical Static Tests: The testing protocol included three cycles, each constituted of 13 blocks with increasing pressure P from 0 to 0.6 bar and then decreasing back to 0 bar. Every block consisted of a pressure step of 0.1 bar at a pressure rate of $\approx 1.5\ \text{bar s}^{-1}$ and a pause of 10 s at constant pressure conditions to evaluate the steady-state behavior. A pause of 30 s was taken between each cycle to ensure the recovery of initial conditions. Three different finger samples were tested for each integration configuration (TOP, MIDDLE, and BOTTOM). One finger sample for NEUTRAL configuration was tested to confirm the predictions of the neutral bending plane position provided by the FEM analysis. For each pressure step block, 1.5 s at the beginning and the end were removed with postprocessing to eliminate transitory data, to take into account the average sensor delay to reach a stabilized signal condition. The data were averaged within the same pressure step of either the loading or unloading part of the cycles of each finger sample and then normalized over the maximum resistance value. Eventually, the R_{norm} of the three finger samples for each integration configuration were averaged. The maximum hysteresis percentage error $H_{max\%}$ was evaluated by comparing the loading and unloading cycles of the averaged data of each integration configuration, as reported in Equation (12),[51] where R_{norm_load} is the R_{norm} value during the loading cycle and R_{norm_umload} of the unloading cycle. Before the beginning of the static test for each new sample, ten dynamic loading and unloading cycles at a speed of $20°\ \text{s}^{-1}$ were carried out on each finger to avoid the Mullins effect.

$$H_{max\%} = \max\left(|R_{norm\_load}| - |R_{norm\_unload}|\right) \cdot 100 \tag{12}$$

Finger Characterization: Electromechanical Dynamic Tests: Three finger samples for each integration configuration of the sensor were tested at four different angular rates (5°, 10°, 20°, and $50°\ \text{s}^{-1}$). The testing protocol for each angular rate included five cycles from $P = 0$ bar to $P_{max} = 0.6$ bar, which corresponded to $\approx\theta = 120°$ and a pause of 30 s at the end of each angular rate block. The lengths of each cycle were 24, 12, 6, and 2.4 s for the four angular rates, respectively. The data related to the first cycle of each angular rate were excluded with post-processing. The data reported for each integration configuration of the sensor were averaged over the three tested finger samples.

Finger Characterization: Calibration Curve: Data interpolation of electromechanical static and dynamic tests of the three finger samples in integration configuration MIDDLE was performed by fitting a polynomial function to the dataset with the Curve Fitter tool available in MATLAB software (MathWorks Inc., Natick, MA, USA). A constraint was applied to ensure the curve passed through the origin (0, 0). The resulting polynomial fit was used to define and visualize the relationship between the normalized resistance value R_{norm} of the sensor and the bending angle of the finger.

Finger Characterization: Electromechanical Fatigue Tests: Three finger samples in the sensor integration configuration MIDDLE were tested from $P = 0$ bar to $P_{max} = 0.6$ bar for 150 cycles, plus 150 cycles after a 20 min pause. The angular rate was $20°\ \text{s}^{-1}$, which represents the operation angular rate of a common pneumatic soft gripper.[33]

Supporting Information

Supporting Information is available from the Wiley Online Library or from the author.

Acknowledgements

G.D.L., M.M., and M.C. acknowledge funding from the European Commission, Horizon Europe Research and Innovation Action under grant agreement no. 101057309, AINCP Project. R.P., N.P., M.M., and M.C. acknowledge funding from the European Union's Horizon 2020 under grant agreement no. 101017054, SoftGrip project. A.C. Bressi acknowledges the funding of Ph.D. grant from Programma Operativo Nazionale - PON "Green" Research and Innovation (CCI 2014IT16M2OP005) and from Ministry of Education, University and Research, Italy, and FSE React-EU. F.G. acknowledges the support of the BRIEF "Biorobotics Research and Innovation Engineering Facilities" project (project identification code IR0000036) funded under the National Recovery and Resilience Plan (NRRP), Mission 4 Component 2 Investment 3.1 of Italian Ministry of University and Research funded by the European Union, NextGenerationEU. F.G. acknowledges funding by the Italian Ministry of Research, under the PNC complementary actions to the NRRP "Fit4MedRob, Fit for Medical Robotics" grant (#PNC0000007). The authors thank Dr. M. Manti and Dr. H. Gomez Bernal from the Institute of Biorobotics at Scuola Superiore Sant'Anna for their help and expertise with mechanical tests. The authors thank R. Di Leonardo and M. Ibrahimi from the Institute of Biorobotics at Scuola Superiore Sant'Anna for their help and expertise with electrical components.

Open access publishing facilitated by Scuola Superiore Sant'Anna, as part of the Wiley - CRUI-CARE agreement.

Conflict of Interest

The authors declare no conflict of interest.

Author Contributions

Giovanna De Luca: conceptualization (equal); data curation (lead); formal analysis (equal); investigation (lead); methodology (equal); validation (lead); visualization (lead); writing—original draft (lead); writing—review and editing (lead). **Anna Chiara Bressi**: conceptualization (equal); data curation (lead); formal analysis (equal); investigation (lead); methodology (equal); validation (lead); visualization (lead); writing—original draft (lead); writing—review and editing (lead). **Radan Pathan**: data curation (supporting); investigation (supporting); methodology (supporting). **Niccolò Pagliarani**: data curation (supporting); formal analysis (supporting); investigation (supporting); validation (supporting); visualization (supporting); writing—original draft (supporting). **Martina Maselli**: methodology (equal); project administration (supporting); supervision (supporting); validation (supporting); writing—review and editing (supporting). **Francesco Greco**: conceptualization (lead); data curation (supporting); funding acquisition (lead); methodology (supporting); project administration (lead); resources (lead); supervision (lead); writing—review and editing (lead). **Matteo Cianchetti**: conceptualization (lead); data curation (supporting); funding acquisition (lead); methodology (supporting); project administration (lead); resources (lead); supervision (lead); writing—review and editing (lead). **Giovanna De Luca** and **Anna Chiara Bressi** contributed equally to this work.

Data Availability Statement

The data that support the findings of this study are available from the corresponding author upon reasonable request.

Keywords

laser-induced graphene, proprioceptions, sensors, soft robotics, stretchable

Received: December 9, 2024
Revised: January 28, 2025
Published online:

[1] Z. Samadikhoshkho, K. Zareinia, F. Janabi-Sharifi, in *2019 IEEE Canadian Conf. Electrical and Computer Engineering (CCECE)*, IEEE, Piscataway, NJ **2019**, pp. 1–4.

[2] J. Shintake, V. Cacucciolo, D. Floreano, H. Shea, *Adv. Mater.* **2018**, *30*, 1707035.

[3] C. Hegde, J. Su, J. M. R. Tan, K. He, X. Chen, S. Magdassi, *ACS Nano* **2023**, *17*, 15277.

[4] G. Gerboni, A. Diodato, G. Ciuti, M. Cianchetti, A. Menciassi, *IEEE/ASME Trans Mech.* **2017**, *22*, 1881.

[5] B. Zazoum, K. M. Batoo, M. A. A. Khan, *Sensors* **2022**, *22*, 4653.

[6] J. Qu, G. Cui, Z. Li, S. Fang, X. Zhang, A. Liu, M. Han, H. Liu, X. Wang, X. Wang, *Adv. Funct. Mater.* **2024**, *34*, 2401311.

[7] H. Wang, M. Totaro, L. Beccai, *Adv. Sci.* **2018**, *5*, 1800541.

[8] S. Sareh, Y. Noh, M. Li, T. Ranzani, H. Liu, K. Althoefer, *Smart Mater. Struct.* **2015**, *24*, 125024.

[9] H. Zhao, K. O'Brien, S. Li, R. F. Shepherd, *Sci. Rob.* **2016**, *1*, eaai7529.

[10] O. D. Yirmibesoglu, Y. Menguc, in *2016 IEEE Inter. Conf. Automation Science and Engineering (CASE)*, IEEE, Piscataway, NJ **2016**, pp. 798–804.

[11] T. Helps, J. Rossiter, *Soft Rob.* **2018**, *5*, 175.

[12] H. A. Wurdemann, S. Sareh, A. Shafti, Y. Noh, A. Faragasso, D. S. Chathuranga, H. Liu, S. Hirai, K. Althoefer, in *2015 37th Annual Inter. Conf. IEEE Engineering in Medicine and Biology Society (EMBC)*, IEEE, Piscataway, NJ **2015**, pp. 8026–8029.

[13] R. L. Truby, M. Wehner, A. K. Grosskopf, D. M. Vogt, S. G. M. Uzel, R. J. Wood, J. A. Lewis, *Adv. Mater.* **2018**, *30*, 1706383.

[14] Y. Yang, Y. Chen, *IEEE Rob. Autom. Lett.* **2018**, *3*, 656.

[15] M. Cianchetti, F. Renda, A. Licofonte, C. Laschi, in *2012 4th IEEE RAS & EMBS Inter. Conf. Biomedical Robotics and Biomechatronics (BioRob)*, IEEE, Rome, Italy **2012**, pp. 634–639.

[16] H. Zhang, M. Y. Wang, *Soft Rob.* **2016**, *3*, 3.

[17] N. Farrow, L. McIntire, N. Correll, in *2017 IEEE Inter. Conf. Robotics and Automation (ICRA)*, IEEE, Piscataway, NJ **2017**, pp. 5525–5531.

[18] C. Larson, B. Peele, S. Li, S. Robinson, M. Totaro, L. Beccai, B. Mazzolai, R. Shepherd, *Science* **2016**, *351*, 1071.

[19] M. Luo, E. H. Skorina, W. Tao, F. Chen, S. Ozel, Y. Sun, C. D. Onal, *Soft Rob.* **2017**, *4*, 117.

[20] H. Yang, Y. Chen, Y. Sun, L. Hao, *Sens. Actuators A: Phys.* **2017**, *266*, 318.

[21] Z. Lin, Z. Wang, W. Zhao, Y. Xu, X. Wang, T. Zhang, Z. Sun, L. Lin, Z. Peng, *Adv. Intell. Syst.* **2023**, *5*, 2200329.

[22] H. Zhao, J. Jalving, R. Huang, R. Knepper, A. Ruina, R. Shepherd, *IEEE Rob. Autom. Mag.* **2016**, *23*, 55.

[23] J. Chen, J. Zhang, Z. Luo, J. Zhang, L. Li, Y. Su, X. Gao, Y. Li, W. Tang, C. Cao, Q. Liu, L. Wang, H. Li, *ACS Appl. Mater. Interfaces* **2020**, *12*, 22200.

[24] M. Amjadi, K.-U. Kyung, I. Park, M. Sitti, *Adv. Funct. Mater.* **2016**, *26*, 1678.

[25] J. C. Yeo, H. K. Yap, W. Xi, Z. Wang, C.-H. Yeow, C. T. Lim, *Adv. Mater. Technol.* **2016**, *1*, 1600018.

[26] S. S. Banerjee, I. Arief, R. Berthold, M. Wiese, M. Bartholdt, D. Ganguli, S. Mitra, S. Mandal, J. Wallaschek, A. Raatz, G. Heinrich, A. Das, *Appl. Mater. Today* **2021**, *25*, 101219.

[27] A. C. Bressi, A. Dallinger, Y. Steksova, F. Greco, *ACS Appl. Mater. Interfaces* **2023**, *15*, 35788.

[28] A. Dallinger, K. Keller, H. Fitzek, F. Greco, *ACS Appl. Mater. Interfaces* **2020**, *12*, 19855.

[29] J. Li, Y. Liu, L. Yuan, B. Zhang, E. S. Bishop, K. Wang, J. Tang, Y.-Q. Zheng, W. Xu, S. Niu, L. Beker, T. L. Li, G. Chen, M. Diyaolu, A.-L. Thomas, V. Mottini, J. B.-H. Tok, J. C. Y. Dunn, B. Cui, S. P. Paşca, Y. Cui, A. Habtezion, X. Chen, Z. Bao, *Nature* **2022**, *606*, 94.

[30] A. M. Barja, Y. K. Ryu, S. Tarancón, E. Tejado, A. Hamada, A. Velasco, J. Martinez, *ACS Omega* **2024**, *9*, 38359.

[31] Q. Li, T. Wu, W. Zhao, Y. Li, J. Ji, G. Wang, *Compos. Part B: Eng.* **2022**, *240*, 110000.

[32] J. Liu, D. Wu, C. Liu, Q. Wang, H. Wang, *Adv. Mater. Technol.* **2024**, *9*, 2301658.

[33] B. Mosadegh, P. Polygerinos, C. Keplinger, S. Wennstedt, R. F. Shepherd, U. Gupta, J. Shim, K. Bertoldi, C. J. Walsh, G. M. Whitesides, *Adv. Funct. Mater.* **2014**, *24*, 2163.

[34] "Dragon Skin Series, High Performance Silicone Rubber.", https://www.smooth-on.com/product-line/dragon-skin/, (accessed: February **2025**).

[35] D. X. Luong, A. K. Subramanian, G. A. L. Silva, J. Yoon, S. Cofer, K. Yang, P. S. Owuor, T. Wang, Z. Wang, J. Lou, P. M. Ajayan, J. M. Tour, *Adv. Mater.* **2018**, *30*, 1707416.

[36] W. Wang, L. Lu, Z. Li, L. Lin, Z. Liang, X. Lu, Y. Xie, *ACS Appl. Mater. Interfaces* **2022**, *14*, 1315.

[37] X. Chen, Z. Hou, G. Li, W. Yu, Y. Xue, G. Niu, M. Xin, L. Yang, C. Meng, S. Guo, *Nano Energy* **2022**, *101*, 107606.

[38] A. Chhetry, M. Sharifuzzaman, H. Yoon, S. Sharma, X. Xuan, J. Y. Park, *ACS Appl. Mater. Interfaces* **2019**, *11*, 22531.

[39] W. Wang, L. Lu, X. Lu, Z. Liang, H. Lin, Z. Li, X. Wu, L. Lin, Y. Xie, *Nano Res.* **2023**, *16*, 1228.

[40] R. Rahimi, M. Ochoa, W. Yu, B. Ziaie, *ACS Appl. Mater. Interfaces* **2015**, *7*, 4463.

[41] Q. Li, T. Wu, W. Zhao, J. Ji, G. Wang, *ACS Appl. Mater. Interfaces* **2021**, *13*, 37433.

[42] C. B. Teeple, K. P. Becker, R. J. Wood, in *2018 IEEE/RSJ Inter. Conf. Intelligent Robots and Systems (IROS)*, IEEE, Piscataway, NJ **2018**, pp. 1621–1627.

[43] B. Jamil, G. Yoo, Y. Choi, H. Rodrigue, *IEEE Rob. Autom. Lett.* **2021**, *6*, 8694.

[44] J. Morrow, H.-S. Shin, C. Phillips-Grafflin, S.-H. Jang, J. Torrey, R. Larkins, S. Dang, Y.-L. Park, D. Berenson, in *2016 IEEE Inter. Conf. Robotics and Automation (ICRA)*, IEEE, Piscataway, NJ **2016**, pp. 5024–5031.

[45] M. L. Dezaki, R. Sales, A. Zolfagharian, H. Y. Nezhad, M. Bodaghi, *Int. J. Adv. Manuf. Technol.* **2023**, *128*, 4207.

[46] Z. Shen, Z. Zhang, N. Zhang, J. Li, P. Zhou, F. Hu, Y. Rong, B. Lu, G. Gu, *Adv. Mater.* **2022**, *34*, 2203650.

[47] A. Koivikko, E. S. Raei, V. Sariola, M. Mosallaei, M. Mantysalo, in *2017 IEEE SENSORS* **2017**, pp. 1–3.

[48] M. Pan, C. Yuan, H. Anpalagan, A. Plummer, J. Zou, J. Zhang, C. Bowen, *Actuators* **2020**, *9*.

[49] X. Chen, R. Li, G. Niu, M. Xin, G. Xu, H. Cheng, L. Yang, *Chem. Eng. J.* **2022**, *444*, 136631.

[50] W. D. Callister Jr, D. G. Rethwisch, *Callister's Materials Science and Engineering 10th Edition*, John Wiley & Sons, Hoboken, NJ **2020**.

[51] I. Baldoli, M. Maselli, F. Cecchi, C. Laschi, *Smart Mater. Struct.* **2017**, *26*, 104011.

[52] Y.-H. Yen, C.-S. Hsu, Z.-Y. Lei, H.-J. Wang, C.-Y. Su, C.-L. Dai, Y.-C. Tsai, *Micromachines* **2022**, *13*, 1220.

[53] N. Pagliarani, G. Picardi, R. Pathan, A. Uccello, H. Grogan, M. Cianchetti, in *2023 IEEE Inter. Workshop on Metrology for Agriculture and Forestry (MetroAgriFor)*, IEEE, Piscataway, NJ **2023**, pp. 170–175.

[54] G. Saggio, *Sens. Actuators A: Phys.* **2012**, *185*, 53.

[55] Q. Ji, X. Zhang, M. Chen, X. V. Wang, L. Wang, L. Feng, in *2020 IEEE 16th Inter. Conf. Automation Science and Engineering (CASE)*, IEEE, Piscataway, NJ **2020**, pp. 842–848.

[56] R. J. Webster, B. A. Jones, *Int. J. Rob. Res.* **2010**, *29*, 1661.

[57] C.-W. Lee, S.-Y. Jeong, Y.-W. Kwon, J.-U. Lee, S.-C. Cho, B.-S. Shin, *Sens. Actuators A: Phys.* **2022**, *334*, 113320.

[58] T. Raza, M. K. Tufail, A. Ali, A. Boakye, X. Qi, Y. Ma, A. Ali, L. Qu, M. Tian, *ACS Appl. Mater. Interfaces* **2022**, *14*, 54170.

[59] S.-Y. Jeong, Y.-W. Ma, J.-U. Lee, G.-J. Je, B.-S. Shin, *Sensors* **2019**, *19*, 4867.

[60] H. Wang, Z. Zhao, P. Liu, Y. Pan, X. Guo, *ACS Appl. Mater. Interfaces* **2022**, *14*, 41283.

[61] L. Tang, J. Zhou, D. Zhang, B. Sheng, *ACS Appl. Nano Mater.* **2023**, *6*, 17802.

[62] S. Duan, B. Wang, Y. Lin, Y. Li, D. Zhu, J. Wu, J. Xia, W. Lei, B. Wang, *Adv. Intell. Syst.* **2021**, *3*, 2100056.

[63] L. Huang, H. Wang, P. Wu, W. Huang, W. Gao, F. Fang, N. Cai, R. Chen, Z. Zhu, *Sensors* **2020**, *20*, 4266.

[64] Y. Zhang, Y. Zhang, M. Sun, S. Wang, S. Wang, J. Sun, H. Ji, Y. Han, Q. He, P. Li, L. Han, Y. Zhang, *ACS Appl. Nano Mater.* **2024**, *7*, 21170.

[65] Y. Wu, I. Karakurt, L. Beker, Y. Kubota, R. Xu, K. Y. Ho, S. Zhao, J. Zhong, M. Zhang, X. Wang, L. Lin, *Sens. Actuators A: Phys.* **2018**, *279*, 46.

[66] S.-Y. Jeong, J.-U. Lee, S.-M. Hong, C.-W. Lee, S.-H. Hwang, S.-C. Cho, B.-S. Shin, *Nanomaterials* **2021**, *11*, 951.

[67] B. Sun, R. N. McCay, S. Goswami, Y. Xu, C. Zhang, Y. Ling, J. Lin, Z. Yan, *Adv. Mater.* **2018**, *30*, 1804327.

[68] T. Pinheiro, R. Correia, M. Morais, J. Coelho, E. Fortunato, M. G. F. Sales, A. C. Marques, R. Martins, *ACS Nano* **2022**, *16*, 20633.